Journal of Power Sources 196 (2011) 1513–1520

Contents lists available at ScienceDirect

Journal of Power Sources

journal homepage: www.elsevier.com/locate/jpowsour

Cycling degradation of an automotive $LiFePO_4$ lithium-ion battery

Yancheng Zhang [a], Chao-Yang Wang [a,*], Xidong Tang [b]

[a] Electrochemical Engine Center (ECEC), Department of Materials Science and Engineering, and Department of Mechanical and Nuclear Engineering, The Pennsylvania State University, University Park, PA 16802, USA
[b] GM R&D and Planning, General Motors, Mail Code: 480-106-390, 30500 Mound Road, Warren, MI 48090-9055, USA

ARTICLE INFO

Article history:
Received 9 July 2010
Received in revised form 20 August 2010
Accepted 23 August 2010
Available online 22 September 2010

Keywords:
$LiFePO_4$
Lithium-ion battery
Cycling degradation
Electrochemical impedance spectroscopy
Electric-only range

ABSTRACT

Degradation of a high capacity prismatic $LiFePO_4$ cell with deep cycling at elevated temperature of 50 °C is studied by electrochemical impedance spectroscopy as well as capacity and power fading characterization at different test temperatures (45, 25, 0 and −10 °C). Capacity fade after 600 cycles is 14.3% at 45 °C and 25.8% at −10 °C. There is little power fade at 45 °C after 600 cycles, whereas the power fade after 600 cycles is 61.6% and 77.2%, respectively, at 0 and −10 °C. The capacity and power fade evidently becomes more severe at lower temperature. In particular, the power fade at low temperatures (e.g., 0 and −10 °C) rather than capacity loss is a major limitation of the $LiFePO_4$ cell. The primary mechanism for capacity fade is loss of cyclable lithium in the cell resulting from lithium-consuming solid electrolyte interphase (SEI) layer growth and side reactions. The increased interfacial resistance (R_w) due to the catalytic growth of SEI layer on the graphite anode and increased electrolyte resistance are the main sources for power fade.

1. Introduction

Lithium insertion and extraction in a $LiFePO_4$ cathode involve a first-order phase transition between two phases ($FePO_4$ and $LiFePO_4$) [1], even though the two-phase reaction theory was challenged at high temperatures (for instance, heating up to 200 °C [2]) and for nano-particles (<50 nm [3]). Both $FePO_4$ and $LiFePO_4$ phases have low electronic conductivity [4,5], and slow diffusion of lithium ions through the two-phase interface limits the charge and discharge current density [1]. These cause poor power capability and low capacity of $LiFePO_4$ batteries. The electronic conductivity has been significantly increased from 10^{-9}–10^{-10} S cm^{-1} to 10^{-2} S cm^{-1} since 2002 [5] but the mechanism for the enhancement is under debate [6–8]. Extensive literature demonstrates that carbon-coating and decreasing particle size (or increasing specific surface area) are effective approaches to overcome the problem of low electronic and ionic conductivities in $LiFePO_4$ cathode [9–20]. In particular, carbon-coated $LiFePO_4$ (C-$LiFePO_4$) was claimed to achieve high capacity (e.g., 90% or above of the 170 mAh g^{-1} theoretical capacity) and excellent cycling performance [10–12]. The attractive properties of C-$LiFePO_4$ as a cathode material have enabled a high-power lithium-ion battery with high safety, low cost and long life, and its commercialization can offer wide applications especially to hybrid electric vehicles (HEVs) and plug-in HEVs (PHEVs).

Excellent long-term cycling stability was demonstrated for C-$LiFePO_4$/graphite prismatic cells with capacity loss of only 14% after 6000 charge–discharge cycles [21], where the cells were cycled at 20 °C and around 1*C* rate. However, high-temperature cycling significantly accelerated capacity fading [22]. Amine et al. reported that there was little capacity fade at 25 °C, but approximately 70% capacity loss at 55 °C after 100 charge–discharge cycles at *C*/3 rate [22]. The fast fading at high temperatures was found to result from formation and growth of thick interfacial film and concomitant large impedance rise on the graphite anode which was catalyzed by iron deposition on the graphite anode subsequent to iron dissolution from the $LiFePO_4$ cathode [22–24]. As per this mechanism, using $Li_4Ti_5O_{12}$ anode instead of graphite anode slowed down iron deposition on the anode with a high potential of ca. 1.5 V versus Li^+/Li [22], and ion-sieving metal coating (30–50 nm Au or Cu coating) on graphite anode reduced solid electrolyte interphase (SEI) formation on the graphite surface [24]. Both approaches greatly improved the cycling performance of $LiFePO_4$ cells at 55 °C. Another solution was to significantly suppress the iron dissolution from the $LiFePO_4$ cathode, for example, by substituting lithium bis(oxalato)borate (LiBOB) for $LiPF_6$ salt [22,25], or introducing an additive of vinylene carbonate (VC) (2 wt%) into the electrolyte [23].

In the present work, a prismatic $LiFePO_4$-based cell with high capacity (16.4 Ah) is explored to study cell degradation through accelerated cycling under a typical PHEV condition (high current rate and deep depth of discharge at elevated temperature). This research provides an improved understanding of the degradation and cycle life of high capacity battery in automotive applications. The cycling degradation was examined through characterization

* Corresponding author. Tel.: +1 814 863 4762; fax: +1 814 863 4848.
E-mail address: cxw31@psu.edu (C.-Y. Wang).

0378-7753/$ – see front matter © 2010 Elsevier B.V. All rights reserved.
doi:10.1016/j.jpowsour.2010.08.070

tests on capacity fade, power fade, electrochemical impedance spectroscopy (EIS), and electric-only range under the US Environmental Protection Agency (EPA) Urban Dynamometer Driving Schedule (UDDS) at different test temperatures (45, 25, 0 and −10 °C). Our goal is to employ the in situ experiments to investigate the possible degradation mechanisms of a $LiFePO_4$-based battery after accelerated cycling. These in situ characterizations provide little direct physical examination like postmortem analysis, but are powerful and convenient diagnostic analysis of the degradation of an automotive battery. Furthermore, these experimental data and degradation analysis are needed to ultimately develop a model-based estimator of state of health (SOH) and state of life (SOL) of an automotive $LiFePO_4$ battery.

2. Experimental

A prismatic $LiFePO_4$-based cell, consisting of C-$LiFePO_4$ cathode and graphite anode, had a nominal capacity of 16.4 Ah with cell dimensions of 232 mm long, 150 mm wide, 6.8 mm thick, and a weight of 500 g. The cell was cycled at 3*C* rate (for both charge and discharge) between 2.0 and 3.6 V at 50 °C. The cycling was interrupted every 300 cycles for characterization tests at different temperatures (in the order of 45, 25, 0 and −10 °C). The characterization tests at each temperature were performed in the following sequence: capacity measurement, electrochemical impedance spectroscopy (EIS), pulse discharge/charge, and electric-only range over the US EPA UDDS driving schedule. Solartron SI 1287 electrochemical interface and Solartron SI 1255B frequency response analyzer (FRA) were coupled for EIS measurement. All the other characterization tests and cycling tests were completed utilizing an Arbin BT-2000 battery cycler. A Tenney Environmental Chamber (with Watlow Series 942 Controller) was adopted to provide constant temperature environment for all the tests. In order for the cell to reach a thermal equilibrium before testing, the cell was kept for 4 h rest at each temperature except at 25 °C for at least 1 h.

Before and after the cycling test (every 300 cycles), capacity characterization was performed at different temperatures (45, 25, 0 and −10 °C) to investigate the capacity fade. The capacity at 1*C* rate was measured in four steps: (1) charging to 3.6 V at constant current of 1*C* rate (16.4 A); (2) holding a constant voltage at 3.6 V until the current dropped to *C*/20 (0.82 A); (3) 10–40 min rest; (4) discharging at 1*C* rate to a cell cut-off voltage of 2.0 V. Rest time between the charging and discharging was 10 min at 50 and 25 °C, 20 min at 0 °C, and 40 min at −10 °C in order for the cell to approach a diffusion equilibrium state.

Electrochemical impedance spectroscopy (EIS) and pulse discharge/charge were carried out at 70% state of charge (SOC) after removing 30% of the present full capacity at 1*C* rate. After 1-h rest at 70% SOC, the impedance spectra were then measured at the open-circuit voltage (OCV) with an AC amplitude of 2 mV over a frequency range from 5000 to 0.005 Hz (10 points per decade of frequency). The low AC amplitude (2 mV) was experimentally selected to accommodate very small impedance in the cell. Then after at least 10-min rest, pulse discharge/charge was performed consecutively at 2*C* rate for different pulse durations: 2 s discharge/2 s rest/2 s charge/30 s rest, and directly 10 s discharge/10 s rest/10 s charge/30 s rest, and then 30 s discharge/30 s rest/30 s charge/30 s rest. The cut-off voltages were 3.8 and 1.6 V. The 2*C* rate here was appropriately chosen for all the testing temperatures down to −10 °C in order to compare the influence of temperature. Variation of the pulse response with cycling is aimed to assess power fade.

The US EPA UDDS driving schedule provides a typical speed profile representative of city driving conditions, from which a cell-scaled power profile with driving time was extracted. The cell was tested over the power profile from 80% SOC to 30% SOC (with respect to the present full capacity) and thus electric-only range was obtained.

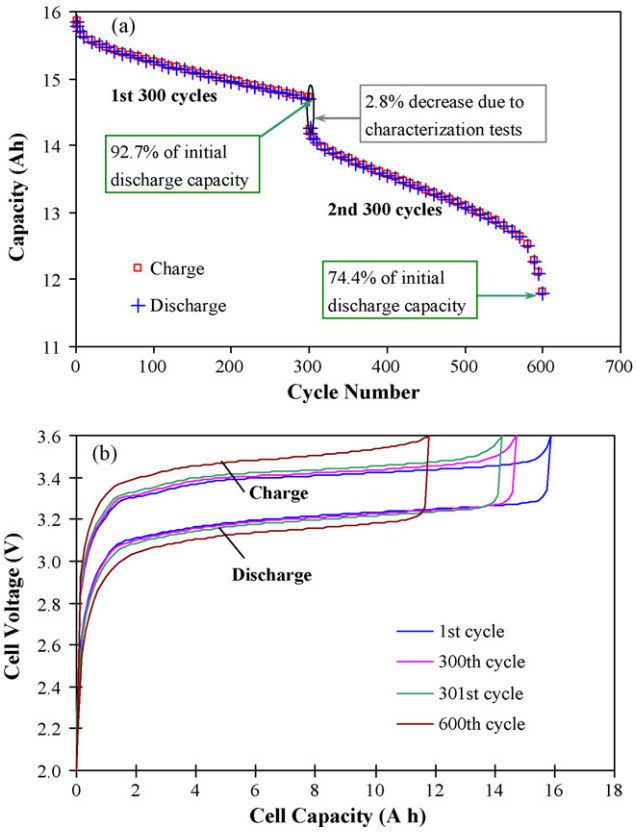

Fig. 1. Cycling performance at 3*C* rate between 3.6 and 2.0 V at 50 °C: (a) cycling capacity versus cycle number; (b) charge–discharge loops for the beginning and last cycles of the 1st 300 cycles (1st and 300th cycles) and the 2nd 300 cycles (301st and 600th cycles).

3. Results and discussion

3.1. Capacity fade

Accelerated cycling test (charging to 3.6 V and discharging to 2.0 V continuously, both at 3*C* rate) was performed at 50 °C. The cycling capacity slowly fades with cycle number, as shown in Fig. 1(a), but declines quickly near the end of the 2nd 300 cycles with 74.4% capacity retention after totally 600 cycles. There is 2.8% capacity loss between the 300th and 301st cycles, which arises from a number of characterization tests between them. Fig. 1(b) shows the charge–discharge loops in the cycling test for the beginning and last cycles of the 1st and 2nd 300 cycles. It is clearly seen that the discharge capacity in the cycling test is very close to the charge capacity. The coulombic efficiency is kept between 99.8% and 100% for the entire 600 cycles; and correspondingly, the energy efficiency declines from 94.1% to 89.6% with cycling.

Charge–discharge curves at 1*C* rate measured at different temperatures (45, 25, 0 and −10 °C) for a fresh cell (before cycling) are shown in Fig. 2(a). The discharge curves present quick voltage decrease at the beginning and near the end, but a flat voltage portion (with a voltage decrease by less than 0.2 V) for a broad capacity range in the middle part. The flat voltage portion is the difference between the voltage plateau at the $LiFePO_4$ cathode (3.5 V corresponding to the Fe^{3+}/Fe^{2+} redox energy in $LiFePO_4$ below the

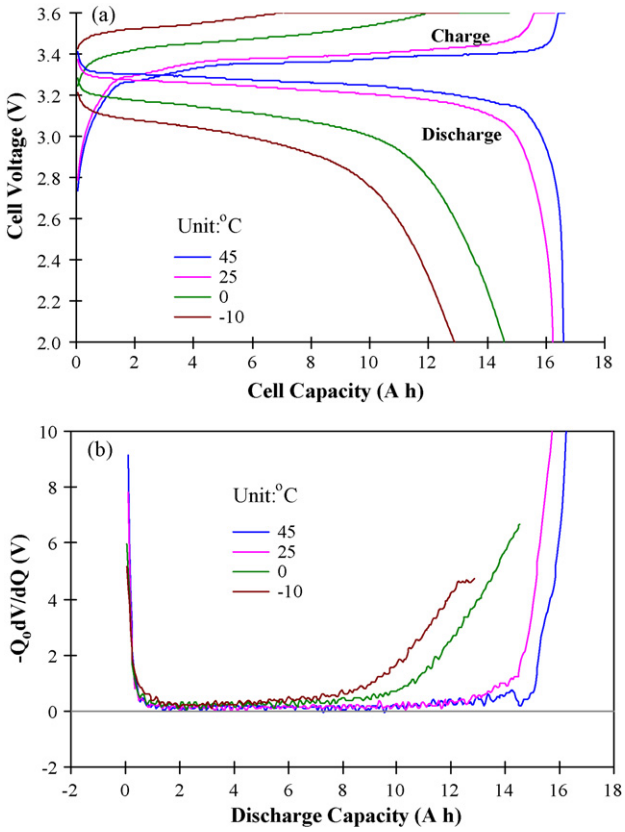

Fig. 2. (a) Charge–discharge curves at 1*C* rate measured at different temperatures for a fresh cell and (b) the corresponding differential voltage ($-Q_o dV/dQ$) versus discharge capacity.

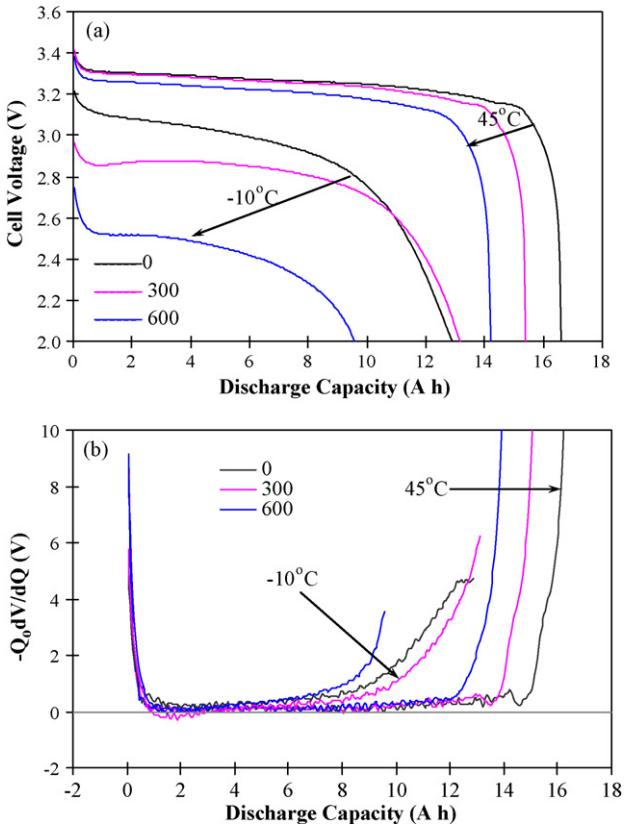

Fig. 3. (a) Discharge curves at 1*C* rate measured at 45 and −10 °C after different cycles and (b) the corresponding differential voltage ($-Q_o dV/dQ$) with respect to discharge capacity.

Fermi level of lithium [26]) and the voltage plateaus at the graphite anode [27], in addition to interfacial polarization and ohmic voltage drop. Staging voltage plateaus at the graphite anode theoretically exist between 0.22 and 0.1 V versus Li corresponding to the coexistence of two phases (e.g., LiC_6–$Li_{0.5}C_6$, $Li_{0.5}C_6$–$Li_{0.33}C_6$ etc.) [28], but are not distinctively observed in Fig. 2(a) due to small difference between staging voltages and plateau sloping caused by various overpotentials [28] at 1*C* rate. The cathode plateau is characteristic of the coexistence of two phases inside the $LiFePO_4$ particles where the two-phase interface moves during the lithium extraction/insertion processes [1,21,29,30]. Strong temperature dependence of the flat voltage portion in Fig. 2(a) for a fresh cell is apparently related to interfacial polarization and ohmic voltage drop. It is also seen from Fig. 2(a) that lowering temperature largely decreases the discharge capacity.

The voltage plateaus are exhibited as the minimal (absolute values) of differential voltage ($-Q_o dV/dQ$) [30], as shown in Fig. 2(b). The derivative of voltage versus capacity (dV/dQ) was calculated as an average of two slopes ($\Delta V/\Delta Q$) at the both sides of each data point followed by smoothing as a 3-point moving average, where ΔV and ΔQ are the changes in voltage and capacity within a data logging interval. The factor $-Q_o$ is used to normalize the dV/dQ based on the cell capacity [31].

When the cell is discharged at l*C* rate, differential voltage curves plunge to the close-to-zero plateaus (less than 0.5 V in Fig. 2(b)), and then the close-to-zero plateaus contribute to about 90% of the full discharge capacity measured at 45 and 25 °C. On the other hand, at 0 and −10 °C, the close-to-zero plateaus contribute to approximately 60% of the full discharge capacity because sluggish lithium diffusion at low temperature causes diffusion overpotential to make the differential voltage curves slowly depart from the close-to-zero plateaus. The differential voltage curves at 45 and 25 °C also depart, but steeply, from the close-to-zero plateaus with further lithium insertion into the cathode. This may be explained with depletion of cyclable lithium in the anode and/or of available intercalation sites in the cathode near the end of discharge so that further lithium transport to the cathode may be largely suppressed and thus the differential voltage increases abruptly.

As seen in Fig. 3(a), the discharge capacity measured at 45 °C clearly shows capacity fade with cycling, for example, 7.3% capacity loss after 300 cycles and 14.3% capacity loss after 600 cycles. The main source for the capacity fade at 45 °C is narrowing of the close-to-zero plateau in the differential voltage curves (Fig. 3(b)), which suggests loss of cyclable lithium during the cycling test. This agrees with loss of lithium inventory as the main capacity fade mechanism in earlier reports on $LiFePO_4$ cells [27,32]. The loss of cyclable lithium is supposed to result from lithium-consuming SEI layer growth and side reactions that also consume electrolyte lithium and increase the electrolyte resistance with cycling as proved from the EIS results below.

The discharge capacity measured at −10 °C shows 25.8% loss after 600 cycles but 1.9% gain after 300 cycles from the initial capacity at −10 °C (Fig. 3(a)). The discharge curves show much larger voltage drop with cycling at the beginning of discharge, which is a reason for the capacity fade at −10 °C. Another reason is narrowing of close-to-zero plateau in the differential voltage curves (Fig. 3(b)) with an exception at 300 cycles. This exception possibly comes from the thermal effect (mainly resistive heating within the cell [33]) as a consequence of considerable resistance rise at −10 °C after 300 cycles. The temperature rise from the thermal effect has delayed the imposition of diffusion overpotential and made the

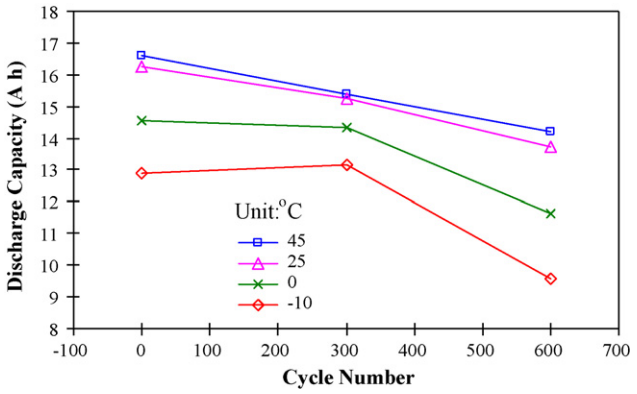

Fig. 4. Discharge capacity measured at different temperatures varying with cycle number.

close-to-zero plateau after 300 cycles be eccentrically longer than the counterpart of a fresh cell at −10 °C.

While capacity test temperature decreases, so does the discharge capacity (Fig. 4). Furthermore, the capacity loss after 600 cycles is found to increase with decrease in capacity test temperature: 14.3% at 45 °C, 15.5% at 25 °C, 20.3% at 0 °C and 25.8% at −10 °C with regard to their respective initial capacity at each temperature.

3.2. Power fade

Pulse discharge and charge at 70% SOC and 2*C* rate was performed consecutively for different pulse durations: 2, 10 and 30 s. The corresponding voltage responses for a fresh cell at different temperatures are shown in Fig. 5. Discharge resistance ($R_{discharge}$) and discharge pulse power capability ($PPC_{discharge}$) are calculated by borrowing the following equations ((1)–(3)) from hybrid pulse power characterization (HPPC) typically for HEV applications [34,35]. The $PPC_{discharge}$ may be used to evaluate power fade with cycling.

$$R_{discharge} = \frac{\Delta V}{\Delta I} = \frac{V_{t_0} - V_{t_1}}{I_{t_0} - I_{t_1}} \quad (1)$$

$$PPC_{discharge} = \frac{V_{min}(OCV - V_{min})}{R_{discharge}} \quad (2)$$

$$PPC_{limit} = V_{min} \times \text{high current limit} \quad (3)$$

In Eq. (1), t_0 is the time point just before each discharge pulse, and t_1 is the time point at the end of each discharge pulse. In Eq. (2), V_{min} is the low cut-off voltage for the discharge current pulse and

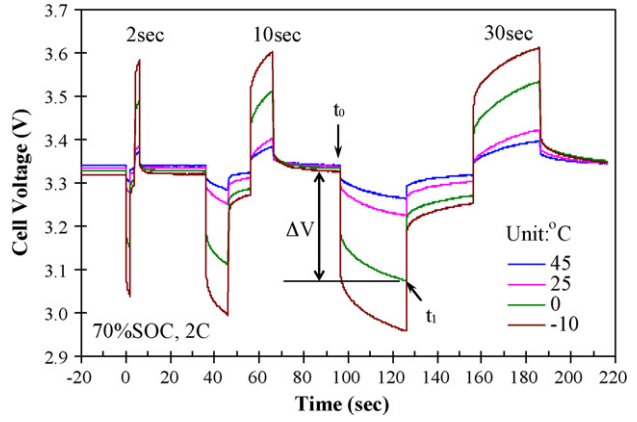

Fig. 5. Cell voltage response to current pulses for different pulse durations (2, 10 and 30 s consecutively) at different temperatures for a fresh cell.

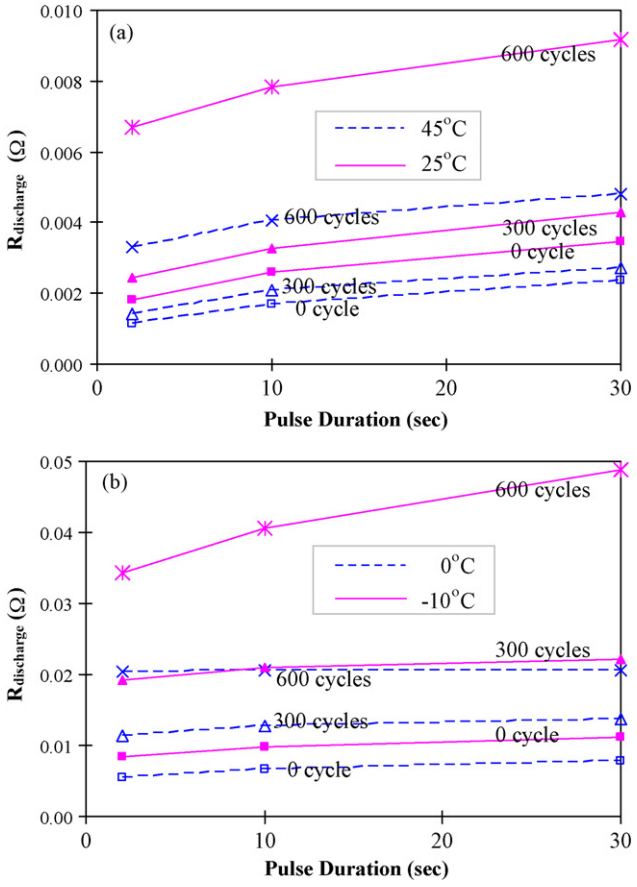

Fig. 6. Discharge resistance ($R_{discharge}$) changes with pulse duration after different cycles (a) at 45 and 25 °C, and (b) at 0 and −10 °C.

OCV is the open-circuit voltage right before the discharge pulse. The OCV before 2 s discharge pulse is a stable measurement value, and is also used as the OCV before 10 and 30 s discharge pulses that is unavailable experimentally due to the lack of relaxation time but may be assumed unchanging after the discharging and charging pulses for each same pulse duration. It is noted that the cell has a limited maximum discharge current at each temperature since serious degradation and even damage may occur above the maximum discharge current. The PPC_{limit} in Eq. (3) determines the possible maximum value for $PPC_{discharge}$. In other words, the $PPC_{discharge}$ is the lower value in the calculation results from Eqs. (2) and (3).

The variation of $R_{discharge}$ with pulse duration and cycle number at different temperatures is shown in Fig. 6(a) and (b). The $R_{discharge}$ drastically increases with cycle number and decreasing temperature, and slowly increases with pulse duration from 2 to 30 s though thermal effect and possible temperature rise from the former pulses may slightly underestimate the resistance for the later pulses owing to the short rest time between pulses. The $R_{discharge}$ for 30 s pulse at 45 °C is, respectively, 2.4, 2.7, and 4.8 mΩ after 0, 300 and 600 cycles, but such resistance increase does not decrease the pulse power capability that is restricted by the PPC_{limit} from 0 to 600 cycles (Fig. 7). Similarly, at 25 °C, the $R_{discharge}$ increases from 3.5 to 4.3 mΩ after 0–300 cycles, and does not decrease the pulse power capability. However, the $R_{discharge}$ increases to 9.2 mΩ after 600 cycles and leads to 16.2% power fade from 300 to 600 cycles. The $PPC_{discharge}$ obtained at 0 and −10 °C is seen to significantly decrease with cycling. The power fade at 0 °C is 42.1% and 61.6%, respectively, after 300 and 600 cycles in comparison with the initial pulse power capability. The power fade at −10 °C is 49.6% and 77.2% after 300 and 600 cycles. Such severe power degradation at low tem-

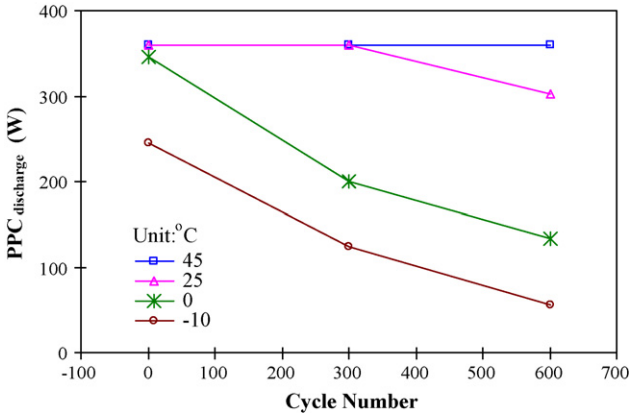

Fig. 7. Discharge pulse power capability ($PPC_{discharge}$) for 30 s pulse as a function of cycle number at different temperatures.

peratures is directly pertinent to greatly increasing $R_{discharge}$ with cycling. For example, the $R_{discharge}$ for 30 s pulse at −10 °C is 11.2, 22.2, and 48.9 mΩ after 0, 300 and 600 cycles, respectively.

3.3. Impedance rise

Electrochemical impedance spectroscopy (EIS) is a powerful in situ characterization technique that is able to probe specific processes in electrochemical systems from the characteristic impedance behaviors along certain frequency ranges. For example, in Fig. 8(a), the impedance spectra present an induction behavior at high frequency, a semi-circular arc at middle frequency and a sloped line like diffusion behavior at low frequency. Furthermore, their changes with cycling can characterize main degradation mechanisms for capacity and power fade.

It is seen from Figs. 8 and 9 that high frequency intercept with the real axis (Z'), representing the ohmic resistance of the cell (R_o), clearly rises with cycle number and lowering temperature. It may be attributable to electrolyte resistance, electronic resistance of electrode particles and current collectors, and connection resistance between the cell terminals and instrument leads [36]. The value of R_o can be as low as a few milliohms (mΩ). For instance,

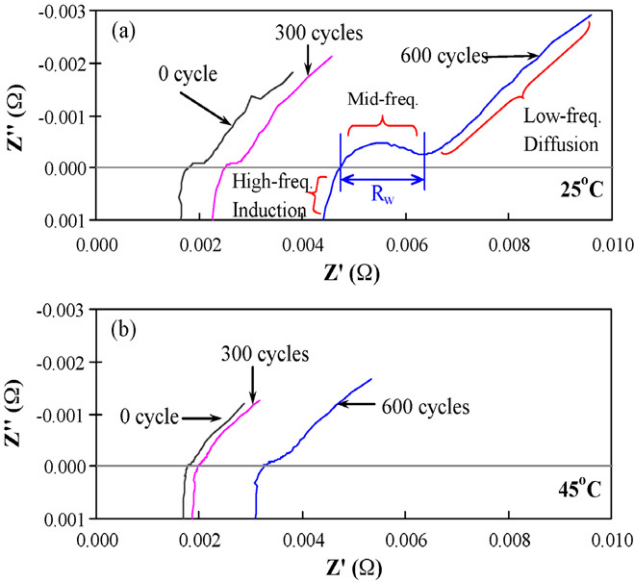

Fig. 8. Nyquist plots of electrochemical impedance spectra measured at 70% SOC after different cycles (a) at 25 °C and (b) at 45 °C.

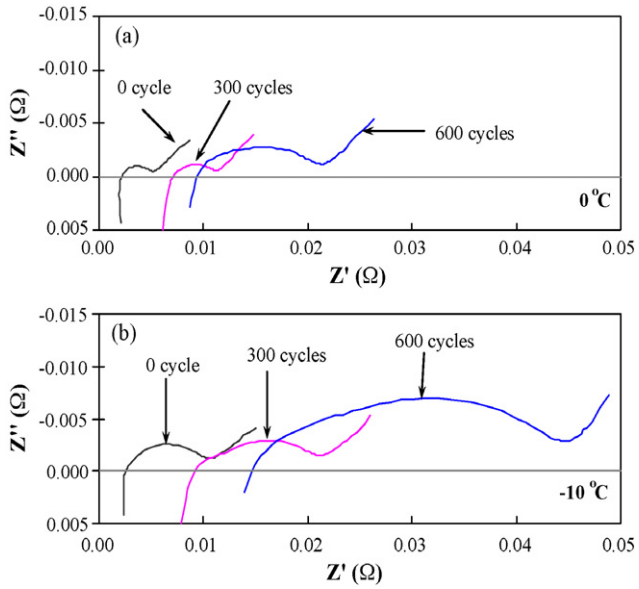

Fig. 9. Nyquist plots of electrochemical impedance spectra measured at 70% SOC after different cycles (a) at 0 °C and (b) −10 °C.

when measured at 45 °C, it is only 1.8, 2.0 and 3.3 mΩ after 0, 300 and 600 cycles, and these apparently show rising tendency with cycle number. It is notable that a special design of screw-tight and surface-to-surface contact was used for excellent connection between the cell terminals and instrument leads that contributed to negligible resistance. Consequently, the EIS measurement is able to accurately detect such small ohmic resistance (such as 1.8 mΩ) without the disturbance of connection resistance.

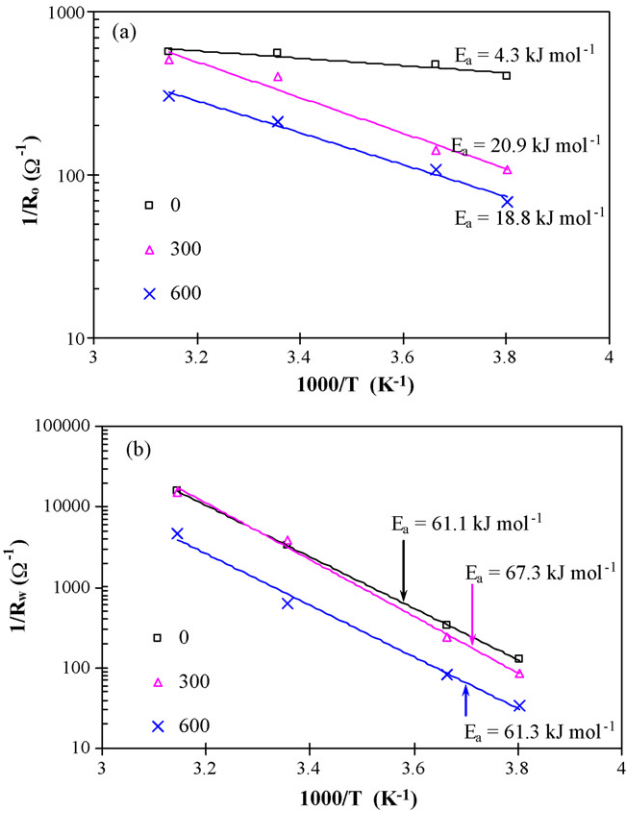

Fig. 10. (a) Lg($1/R_o$) and (b) lg($1/R_w$) follows linear relationship with $1/T$ after different cycles.

The temperature dependence of $1/R_o$ is analyzed by the Arrhenius equation in the form of $(1/R_o) \propto \exp(-E_a/T)$. $\mathrm{Lg}(1/R_o)$ follows a linear relationship with $1/T$ (Fig. 10(a)) and from the linear slope the activation energy (E_a) is obtained as 4.3 kJ mol^{-1} (or 45 meV) for a fresh cell, and increases radically to 20.9 kJ mol^{-1} after 300 cycles but decreases slightly to 18.8 kJ mol^{-1} after 600 cycles. The very low activation energy (45 meV) for a fresh cell is in close agreement with the activation energy of high conductivity of $LiFePO_4$ particles in the literature, such as 60–80 meV in [5] and 30–40 meV in [8], and this may suggest that the electronic resistance of electrode particles (mainly $LiFePO_4$ cathode particles since the anode graphite particles have much higher electronic conductivity) is a dominant factor in the ohmic resistance (R_o) for a fresh cell. The remarkable increase (from 4.3 to 20.9 kJ mol^{-1}) of the activation energy from 0 to 300 cycles implies that increasing electrolyte resistance has become dominant in R_o due to lithium loss in the electrolyte that was consumed in the SEI layer growth and other side reactions. The implied high activation energy for the electrolyte resistance (or ionic conductivity of the electrolyte) is consistent with the typical data in the literature (~15 or ~20 kJ mol^{-1} [37,38]).

The depressed semi-circular arc at the middle frequency is related to the capacitive behavior with a parallel resistance on the electrode/electrolyte interface, for instance, double-layer capacitance with a parallel charge transfer resistance and capacitance of SEI layer in parallel with its resistance [36]. The middle frequency arc width (R_w), as labeled in Fig. 8(a), significantly increases with cycle number and lowering temperature (Figs. 8 and 9). $\mathrm{Lg}(1/R_w)$ reduces linearly with $1/T$, as shown in Fig. 10(b). Fitting with the Arrhenius equation yields the activation energy of 61.1, 67.3 and 61.3 kJ mol^{-1} after 0, 300 and 600 cycles, respectively. Their small difference suggests that the nature of interfacial impedance changes little with cycling. The mid-frequency arc width (R_w) does not greatly increase (0.9–1.5 times at different temperatures) from 0 to 300 cycles, but evidently increases (2.5–6 times at different temperatures) from 300 to 600 cycles. The large increase of R_w from 300 to 600 cycles can be interpreted as the increase of interfacial resistance that is induced by the catalytic growth of SEI layer on the graphite anode due to iron impurities that deposit on the anode after chemical dissolution of iron from the $LiFePO_4$ cathode reacting with HF present in $LiPF_6$ solutions [22–24,27,32,39]. In contrast, the small change of R_w from 0 to 300 cycles shows that the catalytic effect of iron deposition on the anode is not yet enforced on the SEI layer growth on the anode.

The low frequency 45°-sloped line is characteristic of Warburg impedance spectrum corresponding to semi-infinite diffusion. The sloped lines in Figs. 8 and 9 may deviate from 45° due to the effect of porous structure and particle size distribution on the diffusion-related impedance in the active particles. The diffusion impedance appears from the length of the sloped lines to slightly increase from 0 to 300 cycles and modestly increase from 300 to 600 cycles, which is likely related to a decrease of diffusion active area rather than a decrease of diffusion coefficient due to bulk change in the active particles [39].

3.4. Electric-only range

A cell-scaled power profile under the UDDS driving schedule and the harvested power profiles at different temperatures after 300 cycles are shown in Fig. 11. The harvested profiles with sampling rate of 5 Hz comply with the set UDDS power profile except for a few spikes as labeled in pink ovals in Fig. 11. Such power profile was carried out from 80% SOC, and repetitively run until 30% SOC. The driving distance can be obtained by integrating from the speed profile under the UDDS driving schedule. This driving distance is called electric-only range over the 50% SOC window, as shown in Table 1. The electric-only range decreases with lowering temperature by 1.0% at 25 °C, 13.8% at 0 °C and 25.7% at −10 °C in comparison with that at 45 °C (30.82 mile) for a fresh cell. Also, the electric-only range at 45 °C decreases with cycling, and is 96.6% after 300 cycles and 86.2% after 600 cycles. At 0 and −10 °C, the UDDS test labeled as an asterisk (*) in Table 1 was terminated very early because large resistance brought very low voltage and high discharge current to reach a preset high discharge peak power (for example, the test at −10 °C in Fig. 12). Fig. 12 shows the current and voltage profiles corresponding to the beginning 300 s of the harvested power profiles in Fig. 11 at different temperatures after 300 cycles.

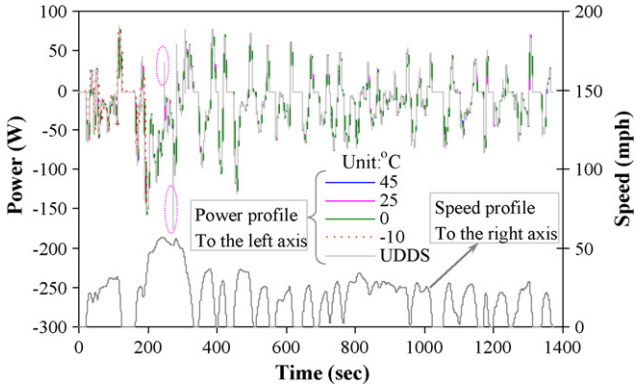

Fig. 11. Speed profile and cell-scaled power profile under the UDDS driving schedule and the harvested power profiles at different temperatures after 300 cycles.

The UDDS tests obey the same power profile with time at all the experimental conditions, and hence the energy (an integration of power with respect to time) per mile is closely comparable (0.84–0.87 Wh mile^{-1} in Table 1 except the early termination occasions) for different cycle numbers and at different temperatures.

The electric-only range is mainly dependent on the cell capacity since the electric-only range is directly proportional to the used

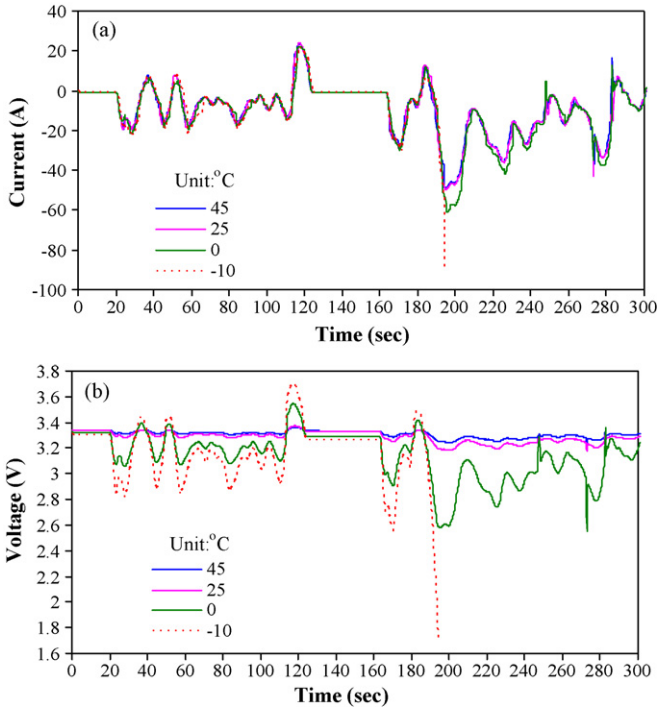

Fig. 12. (a) Current profiles and (b) voltage profiles corresponding to the beginning 300 s of the harvested power profiles in Fig. 11 at different temperatures after 300 cycles.

Table 1
Electric-only range, used capacity and consumed energy under the UDDS driving schedule from 80% to 30% SOC after 0, 300 and 600 cycles (The percentages below are all relative to the value in bold at 45 °C for a fresh cell, and the asterisks symbolize the tests were terminated very early due to power capability too low to surmount a high peak power.).

	Temperature (°C)			
	45	25	0	−10
Electric-only range (mile)				
0	**30.82 (100%)**	30.50 (99.0%)	26.57 (86.2%)	22.89 (74.3%)
300	29.78 (96.6%)	29.20 (94.7%)	24.22 (78.6%)	0.85*
600	26.56 (86.2%)	23.67 (76.8%)	0.84*	–
Used capacity (Ah)				
0	8.157	8.071	7.372	6.581
300	7.713	7.637	7.188	0.300*
600	7.126	6.749	0.305*	–
Used capacity per mile (Ah mile^{-1})				
0	0.265	0.265	0.277	0.288
300	0.259	0.262	0.297	0.353*
600	0.268	0.285	0.363*	–
Consumed energy (Wh)				
0	26.586	26.035	22.643	19.261
300	25.072	24.485	20.922	0.840*
600	22.709	20.622	0.812*	–
Consumed energy per mile (Wh mile^{-1})				
0	0.863	0.854	0.852	0.841
300	0.842	0.839	0.864	0.988*
600	0.855	0.871	0.967*	–
Consumed energy/used capacity (V)				
0	3.259	3.226	3.071	2.927
300	3.251	3.206	2.911	2.800*
600	3.187	3.056	2.662*	–

capacity (the used capacity per mile is 0.26–0.30 Ah mile^{-1} except the values with an asterisk in Table 1). However, the electric-only range per Ah (mile A^{-1} h^{-1}) is reduced by increasing cell resistance because the used capacity per mile (Ah mile^{-1}) exhibits an increasing trend with lowering temperature due to increase in the cell resistance. The influence of cell resistance is extremely exemplified by very small electric-only range with an asterisk in Table 1 that is due to cell resistance too high (power capability too low) to surmount a high discharge peak power. The consumed energy divided by the used capacity is the average voltage under the UDDS tests. The average voltage descends with lowering temperature, which is elucidated by more voltage drop with higher cell resistance.

4. Conclusions

Degradation of a high capacity $LiFePO_4$ cell with deep cycling at elevated temperature of 50 °C is studied by characterizing capacity fade, power fade and impedance rise at different test temperatures (45, 25, 0 and −10 °C). Capacity fade after 600 cycles is 14.3% at 45 °C and 25.8% at −10 °C. The discharge pulse power capability ($PPC_{discharge}$) at 45 °C does not decrease with cycling (namely, there is little power fade) from 0 to 600 cycles, whereas the power fade after 600 cycles is 61.6% and 77.2%, respectively, at 0 and −10 °C. The capacity and power fade evidently becomes more severe at lower temperature due to greatly increasing cell resistance. In particular, the power fade at low temperatures (e.g., 0 and −10 °C) rather than capacity loss is a major limitation of the $LiFePO_4$ cell.

It is found from the variation of the impedance spectra that ohmic resistance (R_o) clearly rises with lowering temperature and upon cycling. The activation energy from the relationship of $\lg(1/R_o)$ with $1/T$ remarkably increases from 4.3 kJ mol^{-1} for a fresh cell to 20.9 kJ mol^{-1} after 300 cycles, which suggests that the electronic resistance of electrode particles is dominant in R_o for a fresh cell and increasing electrolyte resistance has become dominant in R_o after 300 cycles. Accordingly, the increase of ohmic resistance (R_o) with cycling comes mainly from increase in electrolyte resistance resulting from the lithium loss within the electrolyte due to lithium-consuming SEI layer growth and side reactions that also lead to loss of cyclable lithium. Therefore, the loss of cyclable lithium is the primary mechanism for capacity fade, as supported by the narrowing of close-to-zero plateaus in the differential voltage curves. Mid-frequency arc width (R_w) evidently increases (2.5–6 times) from 300 to 600 cycles due to SEI layer growth on the graphite anode with a catalytic effect from iron impurities that deposit from the dissolved iron on the $LiFePO_4$ cathode, but does not greatly increase (0.9–1.5 times) from 0 to 300 cycles because there is no catalytic effect of iron deposition in this period. Consequently, the increased interfacial resistance (R_w) due to the catalytic growth of SEI layer on the anode and increased electrolyte resistance in R_o are the main sources for power fade, leading to very poor discharge pulse power capability at low temperatures (0 and −10 °C) after cycling and even very small electric-only range due to power capability too low to surmount a high discharge peak power under the UDDS driving schedule.

Acknowledgments

Financial support from General Motors is gratefully acknowledged. The authors are thankful to Dr. Richard Steinberger for designing the cell holder and Dr. Christopher D. Rahn for valuable discussions.

References

[1] A.K. Padhi, K.S. Nanjundaswamy, J.B. Goodenough, J. Electrochem. Soc. 144 (1997) 1188.
[2] C. Delacourt, P. Poizot, J.-M. Tarascon, C. Masquelier, Nat. Mater. 4 (2005) 254.
[3] N. Meethong, Y.-H. Kao, M. Tang, H.-Y. Huang, W.C. Carter, Y.-M. Chiang, Chem. Mater. 20 (2008) 6189.
[4] M. Thackeray, Nat. Mater. 1 (2002) 81.
[5] S.-Y. Chung, J.T. Bloking, Y.-M. Chiang, Nat. Mater. 1 (2002) 123.
[6] K. Striebel, J. Shim, V. Srinivasan, J. Newman, J. Electrochem. Soc. 152 (2005) A664.

[7] N. Ravet, A. Abouimrane, M. Armand, Nat. Mater. 2 (2003) 702.
[8] P.S. Herle, B. Ellis, N. Coombs, L.F. Nazar, Nat. Mater. 3 (2004) 147.
[9] Z. Chen, J.R. Dahn, J. Electrochem. Soc. 149 (2002) A1184.
[10] A. Yamada, S.C. Chung, K. Hinokuma, J. Electrochem. Soc. 148 (2001) A224.
[11] H. Huang, S.-C. Yin, L.F. Nazar, Electrochem. Solid-State Lett. 4 (2001) A170.
[12] A.D. Spong, G. Vitins, J.R. Owen, J. Electrochem. Soc. 152 (2005) A2376.
[13] M. Maccario, L. Croguennec, B. Desbat, M. Couzi, F. Le Cras, L. Servant, J. Electrochem. Soc. 155 (2008) A879.
[14] A. Ait Salah, A. Mauger, K. Zaghib, J.B. Goodenough, N. Ravet, M. Gauthier, F. Gendron, C.M. Julien, J. Electrochem. Soc. 153 (2006) A1692.
[15] A.V. Murugan, T. Muraliganth, A. Manthiram, J. Electrochem. Soc. 156 (2009) A79.
[16] J.D. Wilcox, M.M. Doeff, M. Marcinek, R. Kostecki, J. Electrochem. Soc. 154 (2007) A389.
[17] P.P. Prosini, M. Carewska, S. Scaccia, P. Wisniewski, M. Pasquali, Electrochim. Acta 48 (2003) 4205.
[18] Y. Xia, M. Yoshio, H. Noguchi, Electrochim. Acta 52 (2006) 240.
[19] M. Maccario, L. Croguennec, F. Le Cras, C. Delmas, J. Power Sources 183 (2008) 411.
[20] B. Wang, Y. Qiu, L. Yang, Electrochem. Commun. 8 (2006) 1801.
[21] M. Takahashi, H. Ohtsuka, K. Akuto, Y. Sakurai, J. Electrochem. Soc. 152 (2005) A899.
[22] K. Amine, J. Liu, I. Belharouak, Electrochem. Commun. 7 (2005) 669.
[23] H.-C. Wu, C.-Y. Su, D.-T. Shieh, M.-H. Yang, N.-L. Wu, Electrochem. Solid-State Lett. 9 (2006) A537.
[24] H.-H. Chang, H.-C. Wu, N.-L. Wu, Electrochem. Commun. 10 (2008) 1823.
[25] K. Xu, S. Zhang, T.R. Jow, W. Xu, C.A. Angell, Electrochem. Solid-State Lett. 5 (2002) A26.
[26] A.K. Padhi, K.S. Nanjundaswamy, C. Masquelier, S. Okada, J.B. Goodenough, J. Electrochem. Soc. 144 (1997) 1609.
[27] M. Dubarry, B.Y. Liaw, J. Power Sources 194 (2009) 541.
[28] M. Winter, J.O. Besenhard, M.E. Spahr, P. Novak, Adv. Mater. 10 (1998) 725.
[29] C.V. Ramana, A. Mauger, F. Gendron, C.M. Julien, K. Zaghib, J. Power Sources 187 (2009) 555.
[30] M.A. Roscher, J. Vetter, D.U. Sauer, J. Power Sources 191 (2009) 582.
[31] I. Bloom, A.N. Jansen, D.P. Abraham, J. Knuth, S.A. Jones, V.S. Battaglia, G.L. Henriksen, J. Power Sources 139 (2005) 295.
[32] K. Striebel, J. Shim, A. Sierra, H. Yang, X. Song, R. Kostecki, K. McCarthy, J. Power Sources 146 (2005) 33.
[33] C. Forgez, D.V. Do, G. Friedrich, M. Morcrette, C. Delacourt, J. Power Sources 195 (2010) 2961.
[34] J. Shim, K.A. Striebel, J. Power Sources 122 (2003) 188.
[35] I. Bloom, S.A. Jones, V.S. Battaglia, G.L. Henriksen, J.P. Christophersen, R.B. Wright, C.D. Ho, J.R. Belt, C.G. Motloch, J. Power Sources 124 (2003) 538.
[36] Y. Zhang, C.-Y. Wang, J. Electrochem. Soc. 156 (2009) A527.
[37] M. Morita, Y. Niida, N. Yoshimoto, K. Adachi, J. Power Sources 146 (2005) 427.
[38] W. Fang, O.J. Kwon, C.-Y. Wang, Int. J. Energy Res. 34 (2010) 107.
[39] M. Koltypin, D. Aurbach, L. Nazar, B. Ellis, J. Power Sources 174 (2007) 1241.